Energy Proceedings
Vol 60, 2025
ISSN 2004-2965

Fault Location of New Energy Transmission Lines Based on Multiple Frequency Signal Injection

Chenhao Zhang[1*], Yaoyuan Ma[1],Guobing Song[1],Ziyang Wang[1],Qing Wan[2],Jieyu Chen[2]

1 College of Electrical Engineering, Xi'an Jiaotong University,

Xi'an 710049, Shaanxi, China

2 Power Research Institute of State Grid Shaanxi Electric Power Co. Ltd,
Xi'an 710100, Shaanxi, China
(Corresponding Author: zhangchenh@xjtu.edu.cn)

ABSTRACT

To address the influence of converter control and transition resistance on traditional fault-location methods for renewable energy export lines, this paper proposes a single-terminal fault location method based on active injection of complex-frequency signals. Leveraging the controllability of a Static Var Generator (SVG), dual characteristic-frequency signals are injected immediately after fault occurrence. Stable injection is achieved through frequency-separation control and constant-current amplitude regulation. Equivalent fault topologies at the characteristic frequencies are established for both phase-to-phase and single-phase-to-ground faults, from which complex-valued distance equations are derived. Considering the long-line effects, a distributed-parameter model is further adopted to construct dual-frequency distance equations, and the Spider Wasp Optimizer (SWO) is introduced to achieve initial-value-independent fault distance estimation. Simulation results in PSCAD/EMTDC demonstrate that the proposed method exhibits strong robustness against transition resistance and is well-suited for high-accuracy fault location in renewable energy export systems.

Keywords: New Energy; Fault Location; Single-Ended Quantities; Dual-Frequency Signal Injection

1. INTRODUCTION

In parallel with the accelerating global energy transition and advancement of the "dual-carbon" targets, the installed share of renewables in power systems has grown significantly[1,2].Renewable sources represented by photovoltaic and wind power are being widely integrated into transmission and distribution networks, predominantly through power-electronic converters. Compared with synchronous machines, the converter-side electrical quantities have controlled phase, leading conventional impedance-based fault-location methods to lose accuracy—and in some cases fail—in the presence of transition resistance or high-penetration renewables. In addition, the equivalent system impedance on the renewable side changes dynamically with the control strategy before and after a fault, violating the superposition assumption and making parameter-identification methods at the power frequency difficult to apply effectively. For new-type power systems, it is therefore necessary to leverage the controllability of power-electronic equipment and develop new fault-location methods to further enhance supply reliability.

In response to the aforementioned challenges, various solutions have been proposed in the literature. The traveling-wave (TW) method leverages the high-frequency transient components generated at fault initiation. Its primary advantages include independence from system operating conditions and rapid response [3,4]. For instance, Reference [5] achieves fault location by constructing a fault distance matrix using traveling-wave information from both ends of the main and branch lines. Reference [6-8] reduces the reliance on reflected wave identification by utilizing the time difference between zero-mode and aerial-mode waves. References [9]、[10] improve the accuracy of traveling-wave fault location through wavefront calibration and analysis of switching transient time differences, respectively. However, the TW method requires extremely high sampling accuracy, is susceptible to wavefront distortion caused by noise, and performs poorly for faults near the relay or those with high impedance, which limits its practical engineering application.

The time-domain differential equation method also utilizes transient quantities and does not rely on a source impedance model. Reference [11] addresses evolving faults by decomposing the event into stages, solving the differential equations via a sliding-window

This is a paper for the 5th Applied Energy Symposium and Forum: Renewable Energy Matrix (REM2025), Oct. 29-31, 2025, Yancheng, China.

least squares algorithm for location. Reference [12] employs the Levenberg-Marquardt algorithm to nonlinearly solve parameters such as fault distance, branch current, and transition resistance, and achieves fault location through sequential searches of line sections and branches.Reference [13] proposes a single-ended time-domain algorithm based on the Bergeron model and a square-wave similarity index. A key limitation of this category of methods is their susceptibility to high-frequency noise, sampling jitter, and channel errors.

Building on these challenges, a line of research starts from the physics and control characteristics of inverter-based resources and revisits fault location within a frequency-domain, impedance-based framework. References [14],[15] both focus on impedance estimation. References [16],[17] utilize sequence-domain characteristics: one constructs independent equations from positive- and negative-sequence impedance disparities, and the other creates dual operating states during faults to accurately calculate line impedance. Reference [18] presents a domain-based ranging method for asymmetrical faults in wind farm feeders by relocating negative-sequence current to boundary nodes and estimating its injection via phase coherence.By capitalizing on the negative-sequence current suppression inherent to inverter-based resources, fault distance equations are formulated using sequence components in studies [19]、[20]. Reference [21] improves traditional single-ended fault location by utilizing the remote power electronic equipment's response in the composite sequence network, establishing a voltage-current relation at the wind turbine terminal.Taken together, these methods rely on controlled power-frequency quantities for analysis and location, making their effectiveness highly dependent on stable control constraints; under extreme fault conditions or substantial retuning of control strategies, their location accuracy degrades and may fall short of reliability requirements in complex scenarios.

To address the foregoing issues, this paper proposes an active-probing, single-terminal fault-distance estimation method tailored to renewable-energy export lines. The approach leverages the controllability of grid-connected inverters to inject dual-frequency probing signals following fault inception, thereby enhancing frequency-domain fault signatures and enabling distance equations solvable from single-terminal measurements. Simulation studies indicate that the method maintains high accuracy and robustness across operating conditions and provides reliable location performance even under high-resistance faults.

2. DUAL FREQUENCY SIGNAL INJECTION STRATEGY

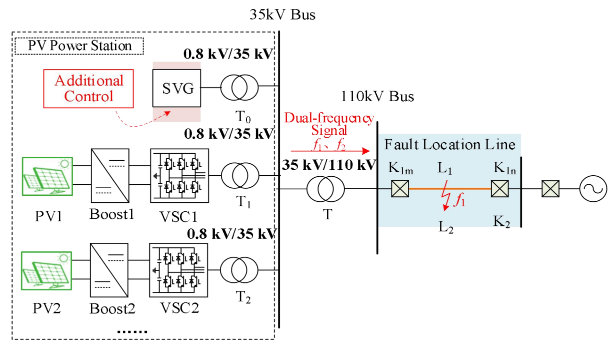

Fig. 1 Photovoltaic station circuit topology

2.1 Injection device selection

When using injected characteristic signals for fault location, relying on coordinated injection by multiple photovoltaic inverters can easily lead to engineering challenges.Firstly, influenced by geographical differences and line reactance The characteristic frequency signals injected by different inverters will generate phase differences when propagating to the bus or transmission line.This phase inconsistency can lead to a "dilution effect" during the signal superposition process,which mean partial cancellation occurs when the injection signals of some inverters are aggregated, resulting in a decrease in the overall signal amplitude on the bus, thereby reducing the observability of fault characteristics.Secondly, Multi-inverter coordinated injection is unreliable.If the control loop of the inverter fails to respond correctly, the effective injection signal capacity for distance measurement will significantly decrease, and the difficulty of extracting and utilizing characteristic frequency electrical quantities will increase.

Therefore, this paper uses SVG as the main feature signal injection source. Because that SVG is essentially equivalent to a large capacity grid connected inverter connected to a 35kV power grid connected to a 35kV bus, it has the strategy of injecting sinusoidal signals with characteristic frequencies using control characteristics.If the SVG fails, coordinated injection by the photovoltaic inverters is activated as a backup injection scheme.

2.2 Converter control strategy

The overall control strategy for dual frequency signal injection based on SVG grid connected inverter is shown in Figure 2

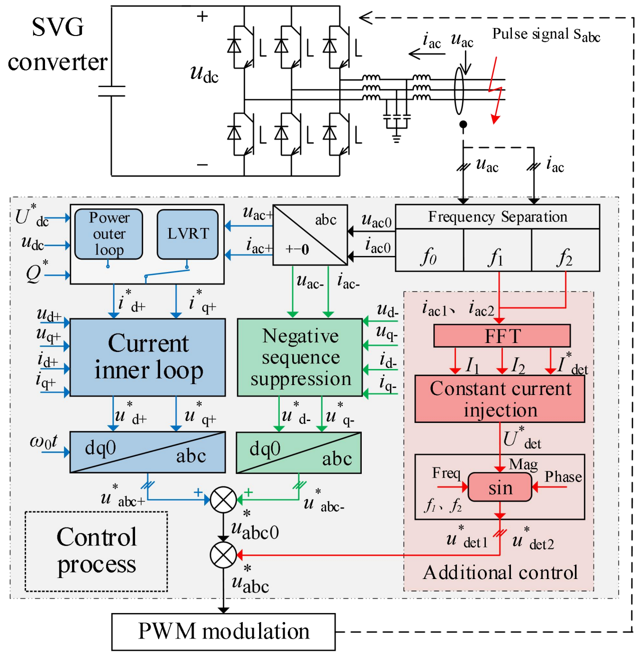

Fig. 2 SVG grid connected inverter control process

2.2.1 Frequency separation stage

Due to the fact that the existing control loop of grid connected inverters is based on a time-domain controller in a synchronous rotating coordinate system, filters are designed to achieve synchronous control of different power frequencies and other frequency signals, reducing the impact on the operation of existing control loops in the injected signal.In order to reduce the duration of the transient process of characteristic frequency signals affected by the power frequency controller during injection, the selected frequency separation loop has the lowest possible delay.

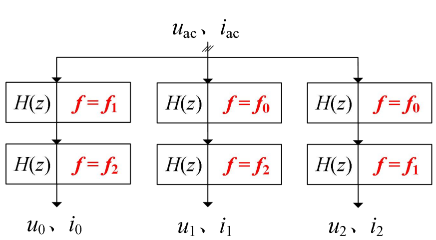

Fig. 3 Frequency separation stage

This stage achieves decoupling control between power frequency and characteristic frequency by using the cascaded frequency separation stage[22]that suppresses IIR type time-domain digital notch filters based on triangular transformation. This structure is shown in Figure 3. The transfer function of IIR type time-domain digital notch filter is as follows:

$$H(z)=h_0\cdot\frac{1-2\cos(n\delta)\cdot z^{-n}+z^{-2n}}{1-2\alpha\cos(n\delta)\cdot z^{-n}+\alpha^2 z^{-2n}} \qquad (1)$$

2.2.2 Additional control steps

ate the objectives of the work and provide an adequate background, avoiding a detailed literature survey or a summary of the result

After the fault, the grid connection point detected the voltage drop and switched to a low voltage ride through strategy. At the same time, the controller initiated an additional injection strategy to achieve positive sequence dual frequency signal injection.

For the amplitude of dual frequency signals, a negative feedback current control loop is designed to limit the current amplitude. The output of the control loop is the voltage amplitude of the characteristic signal. By setting a limiting loop, the injected signal voltage amplitude does not exceed the difference between the rated voltage and the power frequency voltage amplitude. Considering the measurement accuracy error of transformers and the requirements of voltage fluctuation amplitude for power grid operation, the current reference value I^*_{det} for injecting signals is set to 5% of the rated current. The specific control structure diagram is as follows:

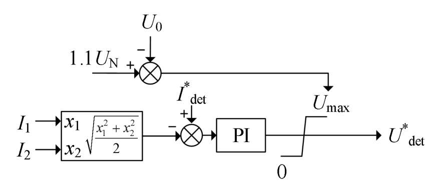

Fig. 4 Constant current amplitude control link

For the frequency of dual frequency signals, the following factors need to be considered: 1.Equipment constraints. The selection of frequency needs to consider the operating frequency band of the transformer, the carrier frequency of the converter, and the adopted frequency of the protection device.2.The selection of frequency requires comprehensive consideration of the amplitude attenuation characteristics of the inverter port filter on the additional characteristic signal.3.In dual frequency injection ranging, the frequency should avoid the power frequency and main harmonics to reduce spectrum leakage and interference.

Maintain moderate intervals to avoid weakening the accuracy of linear equations due to significant differences in impedance characteristics. So the two characteristic frequencies are selected as 225Hz and 325Hz, respectively.

This paper is based on the topology shown in Figure 1 to simulate and verify the injection of additional control characteristic signals in PSCAD/EMTDC. By comparing the dynamic tracking maps of power frequency electrical quantities on the dq axis before and after frequency separation, it found that the power frequency control after frequency separation is not affected by the characteristic frequency, which solves the problem of controller instability caused by the injection of characteristic frequency signals.

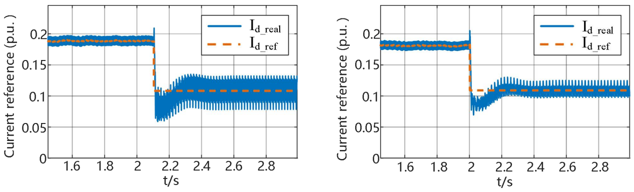

(a)No separation *(b)with separation*

Fig. 5 Comparison of frequency separation stage

After injecting, the electrical quantities at the port of the faulty line are shown in Figure 6. It can be concluded that stable injection of dual frequency signals has been achieved through control strategies.

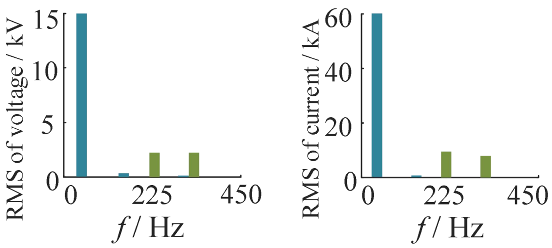

(a) *(b)*

Fig. 6 Frequency separation stage(a)Voltage amplitude-frequency char.(b)Current amplitude-frequency char.

3. FAULT ANALYSIS UNDER CHARACTERISTIC FREQUENCY

3.1 Fault analysis of RL model

When the line is represented by an RL equivalent model, the fault-circuit topologies at the characteristic frequency are constructed for inter-phase faults and for single-phase-to-ground faults, respectively.

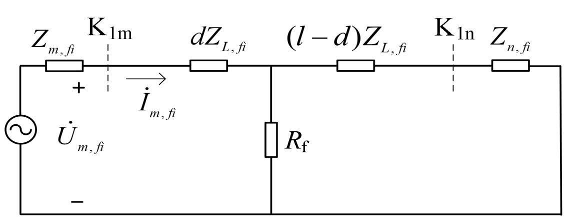

Fig. 7 Equivalent Topology of Characteristic Frequency under Phase-to-Phase Faults

3.1.1 Phase-to-phase fault

For an phase-to-phase fault, the equivalent fault topology at the characteristic frequency is shown in Fig.7. Here, $\dot{U}_{m,fi}$ 、 $\dot{I}_{m,fi}$ denote the inter-phase voltage and current at the characteristic frequency, respectively. At this frequency, we construct a system of equations in four unknowns—the fault distance d, the transition resistance R_f , and the remote-end inductance L_n and resistance R_n . The specific distance-estimation equations are as follows:

$$\frac{\dot{U}_{m,fi}}{\dot{I}_{m,fi}} = dr_l + \mathrm{j}\omega_{fi} dl_l + \frac{R_f(R_n + \mathrm{j}\omega_{fi} L_n)}{R_f + R_n + \mathrm{j}\omega_{fi} L_n} \tag{2}$$

The above is a complex-valued distance equation obtained at a single characteristic frequency. Where ω_{det} is the angular frequency of the injected signal. To avoid the underdetermined nature of the equations, the equations under two characteristic frequencies are established. These equations are presented in linear form with separation into real and imaginary parts as follows, where the subscript *fi* denotes different characteristic frequencies and i=1,2.H_{Re} and H_{Im} denote the real part and the imaginary part of the equation respectively:

$$\begin{cases} H_{Re}(d,R_f,R_n,L_n) = [R_1 \mathrm{Re}(\dot{I}_{m,fi}) - \omega_{fi} L_1 \mathrm{Im}(\dot{I}_{m,fi})]x_1 \\ +\mathrm{Re}(\dot{I}_{m,fi})x_2 + [-\omega_{fi}^2 L_1 \mathrm{Re}(\dot{I}_{m,fi}) - \omega_1 R_1 \mathrm{Im}(\dot{I}_{m,fi})]x_3 \\ -\mathrm{Re}(\dot{U}_{m,fi})x_4 + [-\omega_{fi} \mathrm{Im}(\dot{I}_{m,fi})]x_5 + [\omega_{fi} \mathrm{Im}(\dot{U}_{m,fi})]x_6 = 0 \\ H_{Im}(d,R_f,R_n,L_n) = [R_1 \mathrm{Im}(\dot{I}_{m,fi}) + \omega_{fi} L_1 \mathrm{Re}(\dot{I}_{m,fi})]x_1 \\ +\mathrm{Im}(\dot{I}_{m,fi})x_2 + [-\omega_{fi}^2 L_1 \mathrm{Im}(\dot{I}_{m,fi}) + \omega_1 R_1 \mathrm{Re}(\dot{I}_{m,fi})]x_3 \\ -\mathrm{Im}(\dot{U}_{m,fi})x_4 + [\omega_{fi} \mathrm{Re}(\dot{I}_{m,fi})]x_5 + [-\omega_{fi} \mathrm{Re}(\dot{U}_{m,fi})]x_6 = 0 \end{cases} \tag{3}$$

where x_1-x_6 are defined, respectively, as:

$$x_1 = (R_f + R_n), x_2 = d(R_f + R_n), x_3 = L_n, x_4 = dL_n, x_5 = R_f R_n, x_6 = R_f L_n$$

3.1.2 single-phase-to-ground fault

For single-phase-to-ground faults, a composite sequence network under the characteristic frequency is constructed, as shown in Fig.8. At the characteristic frequency, the positive-sequence and negative-sequence parameters of the remote system can be considered approximately equal. Based on this, fault location equations for the positive-sequence and negative-sequence networks are established.

$$\begin{cases} \dot{U}_{m1} = d\dot{I}_{m1} Z_{l1} + Z_n \dot{I}_{m1} - \dfrac{Z_n}{3R_f}\dot{U}_{mA} + \dfrac{dZ_n}{3R_f}\sum_{j=0}^{2} \dot{I}_{mj} Z_{lj} \\ \dot{U}_{m2} = d\dot{I}_{m2} Z_{l1} + Z_n \dot{I}_{m2} - \dfrac{Z_n}{3R_f}\dot{U}_{mA} + \dfrac{dZ_n}{3R_f}\sum_{j=0}^{2} \dot{I}_{mj} Z_{lj} \end{cases} \tag{4}$$

In the above equation, $Z_n = R_n + j\omega L_n$,which contains the unknown variables to be solved. During the specific solution process, similar linearization processing is performed for the complex equations under dual-frequency injected signals, resulting in the following linear system of equations:

$$\begin{cases} H_{\mathrm{Re}}(d,R_f,R_n,L_n): \sum_{i=1}^{7} A_i x_i = \mathrm{Re}[\dot U_{mj,fi}] \\ H_{\mathrm{Im}}(d,R_f,R_n,L_n): \sum_{i=1}^{7} B_i x_i = \mathrm{Im}[\dot U_{mj,fi}] \end{cases} \tag{5}$$

Here, the variable subscript *j* denotes the positive and negative sequences of electrical quantities,where *j* = 1,2.the real-part equation coefficients A1-A7 and the imaginary-part equation coefficients B1-B7 are respectively as follows:

$$\begin{cases} A_1 = \mathrm{Re}[\dot I_{mj,fi} Z_{lj,fi}], A_2 = \mathrm{Re}[\dot I_{mj,fi}], A_3 = -\omega_{fi}\mathrm{Im}[\dot I_{mj,fi}], \\ A_4 = -\mathrm{Re}[\dot U_{mA,fi}], A_5 = \omega_{fi}\mathrm{Im}[\dot U_{mA,fi}], \\ A_6 = \mathrm{Re}[\sum_{j=0}^{2} \dot I_{mj,fi} Z_{lj,fi}], A_7 = -\omega_{fi}\mathrm{Im}[\sum_{j=0}^{2} \dot I_{mj,fi} Z_{lj,fi}]; \\ B_1 = \mathrm{Im}[\dot I_{mj,fi} Z_{lj,fi}], B_2 = \mathrm{Im}[\dot I_{mj,fi}], B_3 = \omega_{fi}\mathrm{Re}[\dot I_{mj,fi}], \\ B_4 = -\mathrm{Im}[\dot U_{mA,fi}], B_5 = -\omega_{fi}\mathrm{Re}[\dot U_{mA,fi}], \\ B_6 = \mathrm{Im}[\sum_{j=0}^{2} \dot I_{mj,fi} Z_{lj,fi}], B_7 = \omega_{fi}\mathrm{Re}[\sum_{j=0}^{2} \dot I_{mj,fi} Z_{lj,fi}]; \end{cases} \tag{6}$$

The unknowns x_1-x_7 in the above linear system are defined, respectively, as:

$$x_1 = d, x_2 = R_n, x_3 = L_n, x_4 = \frac{R_n}{3R_f}, x_5 = \frac{L_n}{3R_f}, x_6 = \frac{dR_n}{3R_f}, x_7 = \frac{dL_n}{3R_f}$$

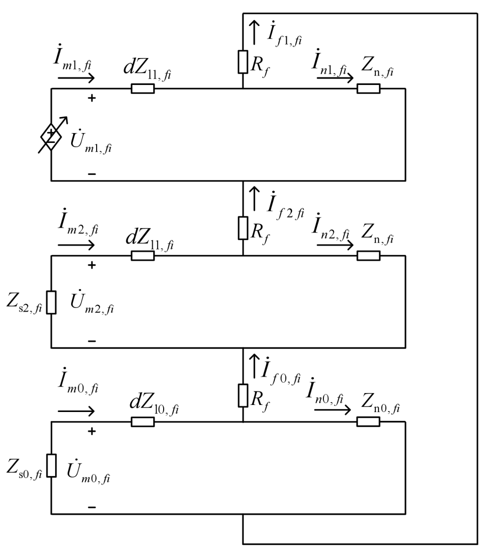

Fig. 8 Composite Sequence Network of Characteristic Frequency under Single-Phase-to-Ground Faults

The above distance-estimation system is rendered overdetermined by forming multiple voltage–current phasor sets via sliding-window sampling, and is subsequently solved using the least-squares method.

3.2 *Fault analysis under distributed parameter model*

3.2.1 Construction of distance measurement equation

Because long-line effects of the line parameters are amplified at the characteristic frequency, a distributed-parameter line model is employed to formulate the distance equations at that frequency so as to reduce fault-location error. For notational simplicity, the hyperbolic dependence on the fault distance is written as follows,Here, γ_1 and γ_0 denote the positive-sequence and zero-sequence line propagation coefficients at the characteristic frequency, respectively:

$$\begin{cases} C_{11} = \cosh(\gamma_1 d), C_{21} = \cosh[\gamma_1(l-d)], C_{10} = \cosh(\gamma_0 d) \\ S_{11} = \sinh(\gamma_1 d), S_{21} = \sinh[\gamma_1(l-d)], S_{10} = \sinh(\gamma_0 d) \end{cases} \tag{7}$$

Combining the transmission-line equations on both sides of the fault with the current relation at the fault branch yields a unified system. The electrical quantities of the remote system under the distributed parameter model can be expressed as the virtual electrical quantities calculated for the healthy line plus the form that contains the fault boundary condition equation *F*,namely:

$$\begin{cases} \dot U_x = \dot U(x) + F S_{21} Z_{ci} \\ \dot I_x = \dot I(x) - F C_{21} \end{cases} \tag{8}$$

Where, for an phase-to-phase fault,take the BC-phase fault as an example,the explicit form of the fault-distance equation is given by:

$$\begin{aligned} &\dot U_{nBC,fi}' + F_{BC,fi} S_{21,fi} Z_{c1,fi} = \\ &(R_n + j\omega_{fi} L_n)(\dot I_{nBC,fi}' - F_{BC,fi} C_{21,fi}) \end{aligned} \tag{9}$$

At this stage, the augmented form $F_{BC,fi}$ of the fault-boundary condition is:

$$F_{BC,fi} = \frac{2[\dot U_{mBC,fi}\cosh(\gamma_{1,fi} l) - Z_{c1,fi}\dot I_{mBC,fi}\sinh(\gamma_{1,fi} l)]}{R_f} \tag{10}$$

For a single-phase-to-ground fault,take the BC-phase fault as an examplethe explicit form of the distance-estimation equation F_1 is as follows:

$$\begin{aligned} &\dot U_{nj,fi}' + F_{AG,fi} S_{21,fi} Z_{c1,fi} = \\ &(R_n + j\omega_1 L_n)(\dot I_{nj,fi}' - F_{AG,f1} C_{21,f1}) \end{aligned} \tag{11}$$

At this point, the supplementary form $F_{AG,fi}$ of the fault boundary condition is

$$F_{AG,fi} = \sum_{j=0}^{2} \frac{\dot U_{mj,fi}\cosh(\gamma_{j,fi} d) - Z_{cj,fi}\dot I_{mj,fi}\sinh(\gamma_{j,fi} d)}{3R_f} \tag{12}$$

The above expressions are respectively the fault location equation sets for dual-frequency injection under phase-to-phase faults and single-phase-to-ground faults. Since the variable to be solved (fault distance d) exists in the form of a hyperbolic function in the equations, and the model adopts a lossy transmission line, the hyperbolic functions in the equations cannot be separated into real and imaginary parts to derive a real-valued equation set with respect to d. Consequently, the least squares method based on overdetermined equations cannot be applied for solution.

3.2.2 Fault distance solving algorithm

To address the above issue, an initial-value-independent heuristic algorithm is applied to the equations, and this paper adopts the Spider Wasp Optimizer (SWO) to solve for the fault distance.

The Spider Wasp Optimizer (SWO) is a novel meta-heuristic intelligent optimization algorithm, inspired by the hunting, nesting, and breeding behaviors of spider wasps in nature[23]. SWO integrates the mechanisms of group search and genetic crossover, featuring stronger global search capability and local exploitation capability.

The specific flow of the algorithm is as follows: First, population individuals are randomly initialized in the solution space, where each individual represents a candidate solution. Subsequently, the iterative update process begins. In each iteration, individuals select to perform either hunting and nesting behaviors or mating behavior with a certain probability. During the hunting phase, individuals move in the search space through methods such as differential step size or cosine perturbation, achieving a balance between exploration and exploitation. Furthermore, SWO introduces a population reduction strategy: as the number of iterations increases, the population size gradually decreases. This ensures strong exploration capability in the early stages while improving convergence accuracy in the later stages.

4. SIMULATION VERIFICATION

A photovoltaic grid-connected system model as shown in Fig. 1 was built in the PSCAD/EMTDC simulation software. The length of the grid-connected outgoing line L1 is set to 100 km, the line model adopts the Bergeron model in PSCAD, and the sampling frequency is 20 kHz. The line parameters are as follows: Positive-sequence resistance r1 = $4.9771\times10^{-2}\Omega$/km; positive-sequence reactance x1 = $3.0940\times10^{-1}\Omega$/km; positive-sequence susceptance b1 = 3.6742×10^{-6} S/km;Zero-sequence resistance r0 = $2.7283\times10^{-1}\Omega$/km; zero-sequence reactance x0 = $7.4776\times10^{-1}\Omega$/km; zero-sequence susceptance b0=2.2156×10^{-6}S/km.

The main parameters of the system are shown in Table 1.

To verify the fault location performance of the proposed fault location method under different fault locations, simulations were conducted for single-phase-to-ground faults and phase-to-phase faults respectively. Additionally, to verify whether the fault location method is affected by transition resistance, transition

Tab 1Main parameters of photovoltaic grid connected system model

Variable	Parameter
Output Power per PV System / MW	2
Quantity of PV Inverters / unit	25
Capacity of SVG / MVA	20
Solar Irradiance Intensity / W/m^2	1200
Temperature / ℃	28
Capacity of Converter Transformer / MVA	70
Transformation Ratio of Step-Up Transformer / kV:kV	110:35
Transformation Ratio of Inverter Outlet Transformer / kV:kV	35:0.69
Capacity of AC Power Grid / MVA	100
SCR	1.25

resistances of 10Ω and 100Ω were set for fault location tests in the scenario of single-phase-to-ground faults, and the same transition resistance values (10Ω and 50Ω) were also applied for fault location in the scenario of phase-to-phase faults. The results are shown in Table 2 and Table 3.

Tab 2 Location results for single-phase-to-ground faults

Fault Type	R_f(Ω)	Fault Distance *d*(km)				
		Actual Value	RL Model		Bergeron Model	
			Measured Value	Error (%)	Measured Value	Error (%)
AG	10	10	10.5623	0.56	10.6510	0.65
		50	49.1527	0.85	50.9905	0.99
		90	91.7321	1.73	91.9361	1.94
	100	10	12.2419	2.24	9.2217	0.78
		50	54.5378	4.54	51.8641	1.86
		90	95.4912	5.49	90.9412	0.94

The fault location simulation results for single-phase-to-ground faults are shown in Table 2. As can be seen from the above simulation results, during single-phase-to-ground faults, when the RL model-based fault location method is adopted, the calculation result errors are relatively large under high-resistance faults. In contrast, when the distributed-parameter line model is used, the proposed fault location method is applicable to the power evacuation lines of new energy stations, is not affected by fault distance or transition resistance, and exhibits high fault location accuracy. The maximum fault location error in the table is less than 2%, which verifies the correctness and accuracy of the method.

The fault location results for phase-to-phase faults are shown in Table 3. By observing the fault location results presented in Table 3, it can be seen that the RL model-based fault location method has errors in fault location under high-resistance faults, while it achieves accurate fault location under low-resistance faults. In contrast, the fault location method using the Bergeron Model has good transition resistance tolerance, and all its fault location errors are less than 2%.Among these, the fault location errors for two-phase short-circuit to ground faults are slightly larger than those for two-phase short-circuit faults.

Tab 3 Fault location results for phase-to-phase faults

Fault Type	R_f(Ω)	Fault Distance *d*(km)				
		Actual Value	RL Model		Bergeron Model	
			Measured Value	Error (%)	Measured Value	Error (%)
BC	10	10	10.1223	0.12	9.9124	0.09
		50	50.6765	0.68	51.2763	1.28
		90	90.7562	0.76	89.1276	0.83
	50	10	11.0007	1.00	10.6542	0.65
		50	53.6708	3.67	51.9810	1.98
		90	94.2640	4.26	91.2202	1.22
BCG	10	10	9.6998	0.30	10.3721	0.37
		50	51.0402	1.04	48.9785	1.02
		90	91.9204	1.92	91.5861	1.59
	50	10	11.0602	1.06	10.6524	0.65
		50	53.0085	3.01	49.1929	0.81
		90	94.2003	4.20	91.1982	1.20

Tab 4 The fault location results affected by noise interference

Fault Type	Fault Distance *d*(km)				
	Actual Value	RL Model		Bergeron Model	
		Measured Value	Error (%)	Measured Value	Error (%)
AG	10	10.1570	0.16	10.0632	0.06
	30	29.8605	0.14	30.6451	0.65
	50	50.9970	1.00	49.1327	0.87
	80	78.3311	1.67	81.2137	1.21
BC	10	9.8924	0.11	10.1287	0.13
	30	30.3427	0.34	30.2567	0.26
	50	51.7562	1.77	49.5765	0.42
	80	83.1201	3.12	81.0050	1.01
BCG	10	10.6127	0.61	9.5668	0.43
	30	29.0875	0.82	31.0603	1.06
	50	48.0203	1.98	51.8224	1.82
	80	82.1252	2.13	80.3167	0.31

To assess the noise robustness of the proposed fault-location method, white noise with a signal-to-noise ratio (SNR) of 30 dB was simultaneously superimposed on the voltage and current measurement channels, with the transition resistance fixed at R_f=30 Ω. Fault locations for various fault types were computed using a 10 ms data window, and the time-averaged estimate was adopted as the final result (see Table 4). Under this noise level, the distance-estimation error was ≤ 4%, demonstrating good robustness to noise. This robustness stems from the inverter's constant-amplitude control at the characteristic frequencies, which ensures stable dual-frequency injection and suppresses high-frequency random components, thereby rendering the method effectively insensitive to typical measurement noise.

5. CONCLUSIONS

The single-terminal fault location method based on dual-frequency active injection using an SVG proposed in this paper is theoretically derived and verified through PSCAD/EMTDC simulations, demonstrating feasibility and accuracy in both injection control and distance estimation under different line models.

1)A low-delay frequency-separation loop and constant-current feedback control enable immediate dual-frequency injection after a fault without disturbing power-frequency operation. The amplitude-limiting mechanism ensures signal observability and equipment safety. Simulations confirm that dq-axis power-frequency quantities remain stable while characteristic components are clearly extractable.

2)Complex distance equations are formulated for phase-to-phase and single-phase-to-ground faults. To account for long-line effects, a distributed-parameter (Bergeron) model is employed in addition to the RL equivalent model. The Spider Wasp Optimizer (SWO) efficiently solves the nonlinear equations without initial-value dependence, achieving robust and accurate fault localization.

ACKNOWLEDGEMENT

This work is supported by the project "Research on Fault Location Technology for Centralized New Energy Transmission Lines Based on Protection-Control Coordination" (No. 5226KY24001A).

REFERENCE

[1] Zhuang G Y. Challenges and countermeasures for China's realization of the "dual-carbon" targets. People's Tribune 2021;18:50–3.

[2] Han X, Li T, Zhang D, et al. New issues and key technologies of new power system planning under the dual carbon goal. High Voltage Engineering 2021;47(9):3036–46.

[3] Liu Z, Gao H, Luo S. Non-unit protection for long-distance LCC-HVDC transmission lines based on waveform characteristics of voltage travelling waves. Electr Power Syst Res 2023;150:108352.

[4] Naidu OD, Pradhan AK. A traveling wave-based fault location method using unsynchronized current

measurements. IEEE Trans Power Delivery 2019;34(2):505–13.
[5] Liu W., Li W., Sun J., et al. Research on Improved Algorithm for Fault Location of Wind Power Collection Lines Based on Multi Terminal Traveling Wave Information. In: 2024 4th International Conference on Intelligent Power and Systems (ICIPS). IEEE; 2024: 375-80.
[6] Wang Z., Ma X., Lu Y., et al. Single-Ended Data Based Fault Location Method for Multi-Branch Distribution Network. Energy Reports. 2020;6: 385-90.
[7] Lin X, Kursan I, Sun J, et al. Accurate single-ended data based fault location method for multi-source and multi-branch distribution network. In: Proceedings of the 12th IET International Conference on Developments in Power System Protection (DPSP 2014); 2014:1-6.
[8] Luo X, Shan H, Zhang L, et al. Fault location on multi-branch network using traveling wave and graph theory. In: 2021 6th Asia Conference on Power and Electrical Engineering (ACPEE); 2021:168-72.
[9] Tong N., Chen L., Wang W., et al. Local Measurement-Based High-Speed Protection for Half-Wavelength UHV Lines. IEEE Transactions on Power Delivery. 2020;35(5): 2481-94.
[10] Shi S., Zhu B., Lei A., et al. Fault Location for Radial Distribution Network via Topology and Reclosure-Generating Traveling Waves. IEEE Transactions on Smart Grid. 2019;10(6): 6404-13.
[11] Kulkarni S., Santoso S. Time-Domain Algorithm for Locating Evolving Faults. IEEE Transactions on Smart Grid. 2012;3(4): 1584-93.
[12] Qin Y, Wang B, Pan B, et al. Phase-to-phase short-circuit fault location for 35 kV distribution lines based on time-domain impedance method. Power System Protection and Control 2025;53(16):169–76.
[13] Wang G., Xu Z., Liang Y., et al. Single Terminal Time Domain Fault Location Method Based on the Similarity of Square Wave for Arc Grounding Fault. Power System Protection and Control. 2012;40(23): 109-13.
[14] Hooshyar A, Azzouz M A, El-Saadany E F. Distance protection of lines emanating from full-scale converter-interfaced renewable energy power plants—Part II: Solution description and evaluation. IEEE Trans Power Deliv 2014;30(4):1781–91.
[15] Paladhi S, Pradhan A K. Adaptive distance protection for lines connecting converter-interfaced renewable plants. IEEE J Emerg Sel Top Power Electron 2021;9(6):7088–98.
[16] Chang P, Song G, Hou J, Xu R. A single-terminal fault location method for transmission lines integrated by inverter-type source. IEEE Trans Power Deliv 2022;37(3):1704–13.
[17] Chang P, Song G, Liu W, et al. Fault line impedance calculation method for inverter-grid-connected systems based on coordinated protection and control. Autom Electr Power Syst 2023;47(22):87–100.
[18] Ding J, Zhu Y L, Wei Y. Asymmetrical fault location scheme for wind farm collection lines based on negative-sequence current relocation. Proc CSEE 2025;45(4):1436–50.
[19] Zhang H, Zheng X, Chao C, et al. Single-phase grounding distance protection for flexible DC AC transmission lines based on comprehensive sequence components. Automation of Electric Power Systems 2024;48(17):119–29.
[20] Chao C, Zheng X, Ye H, et al. A novel MMC-side distance protection scheme for single-phase grounding fault of offshore wind farm collection line. Proceedings of the CSEE 2024;44(15):5899–908.
[21] Song G, Wei W, Zhang C, et al. Exploration of a single-ended fault location method utilizing the response characteristics of remote power electronic equipment. Power System Technology (Published online).(2025).https://link.cnki.net/urlid/11.2410.TM.20250725.1230.012
[22] Song G, Cui X, Zhang C, et al. A precise power-frequency notch filter for abnormal state perception in power systems. Proc 8th Asia Conf Power Electr Eng (ACPEE) 2023:2160–7.
[23] Abdel-Basset M, Mohamed R, Jameel M, et al. Spider wasp optimizer: a novel meta-heuristic optimization algorithm. Artif Intell Rev 2023;56:11675–738.